ULTRAVIOLET IMAGING TELESCOPE AND OPTICAL EMISSION-LINE OBSERVATIONS OF H II REGIONS IN M81

JESSE K. HILL,[1,5] K.-P. CHENG,[1,5] RALPH C. BOHLIN,[2] ROBERT H. CORNETT,[1,5] P. M. N. HINTZEN,[5,6]
ROBERT W. O'CONNELL,[3] MORTON S. ROBERTS,[4] ANDREW M. SMITH,[5]
ERIC P. SMITH,[5] AND THEODORE P. STECHER[5]
Received 1994 May 20; accepted 1994 July 5

ABSTRACT

Images of the type Sab spiral galaxy M81 were obtained in far-UV and near-UV bands by the Ultraviolet Imaging Telescope (UIT) during the Astro-1 Spacelab mission of 1990 December. Magnitudes in the two UV bands are determined for 52 H II regions from the catalog of Petit, Sivan, & Karachentsev (1988). Fluxes of the Hα and Hβ emission lines are determined from CCD images. Extinctions for the brightest H II regions are determined from observed Balmer decrements. Fainter H II regions are assigned the average of published radio-Hα extinctions for several bright H II regions. The radiative transfer models of Witt, Thronson, & Capuano (1992) are shown to predict a relationship between Balmer Decrement and Hα extinction consistent with observed line and radio fluxes for the brightest 7 H II regions and are used to estimate the UV extinction. Ratios of Lyman continuum flux (computed from the extinction corrected Hα flux) to the extinction corrected far-UV flux are compared with ratios predicted by model spectra computed for IMF slope equal to -1.0 and stellar masses ranging from 5 to 120 $M_\odot$. Ages and masses are estimated by comparing the Hα and far-UV fluxes and their ratio with the models. The total of the estimated stellar masses for the 52 H II regions is 1.4×10^5 $M_\odot$. The star-formation rate inferred for M81 from the observed UV and Hα fluxes is low for a spiral galaxy at ~ 0.13 $M_\odot$ yr^{-1}, but consistent with the low star-formation rates obtained by Kennicutt (1983) and Caldwell et al. (1991) for early-type spirals.

Subject headings: dust, extinction — galaxies: individual (M81) — galaxies: stellar content — H II regions — ultraviolet: galaxies

1. INTRODUCTION

Ultraviolet images of spiral galaxies are dominated by the OB/H II complexes in the spiral arms, with the older nuclear bulge population making a significant contribution for early Hubble-type galaxies (e.g., Hill, Bohlin, & Stecher 1984; O'Connell et al. 1992; Bohlin et al. 1990a, 1990b; Hill et al. 1992). The large, nearby Sab spiral galaxy M81 was observed in far-UV and near-UV bands by the Ultraviolet Imaging Telescope (UIT) during the 1990 December Astro-1 Spacelab mission. Ground-based CCD images were subsequently obtained using interference filters centered on the Hα and Hβ emission lines. Images in neighboring continuum bands were also obtained. A log of the observations used in this investigation is given in Table 1.

UIT is a 38 cm Ritchey–Chrétien telescope, which images a 40′ diameter field to the cathode of the selected one of two two-stage magnetically focussed image intensifiers coupled by fiber optics to IIaO film. The intensifiers have UV-sensitive, solar-blind photocathodes. CsTe for the near-UV camera (A) and CsI for the far-UV camera (B). The UIT instrument, the available bandpasses, and the method by which the images are reduced to flux-calibrated arrays are discussed by Stecher et al. (1992). The bandpasses used in this investigation are called A1 (centroid 2490 Å, width 1150 Å) and B1 (centroid 1520 Å, width 354 Å).

Hill et al. (1992) compared A1, B1, and V band radial profiles of M81 and discussed preliminary H II region photometry. Figures 1 and 2 (Plates 9 and 10) show the near-UV and far-UV images used in this investigation. Here, we present and discuss multiband photometry of 52 M81 H II regions from the catalog of Petit, Sivan, & Karachentsev (1988, hereafter PSK). The H II regions investigated are circled on the pictures. Previous studies of the H II regions of M81 also include those of Hodge & Kennicutt (1983), Stauffer & Bothun (1987), Garnett & Shields (1987), and Kaufman et al. (1987).

2. H II REGION PHOTOMETRY AND EXTINCTION CORRECTION

The H II regions are identified on the UIT images with the aid of Figures 1a and 1b of PSK. Except for the nucleus, all localized sources on the far-UV image can be identified as H II regions from PSK. Aperture photometry uses apertures of radius 8 arcsec on the UV images and apertures of radius 7 arcsec on the CCD emission line images. (The apertures are 7 pixels in radius on all images, but the emission line images have a slightly smaller plate scale.) The local sky background is determined as the mode of pixels within annuli whose inner
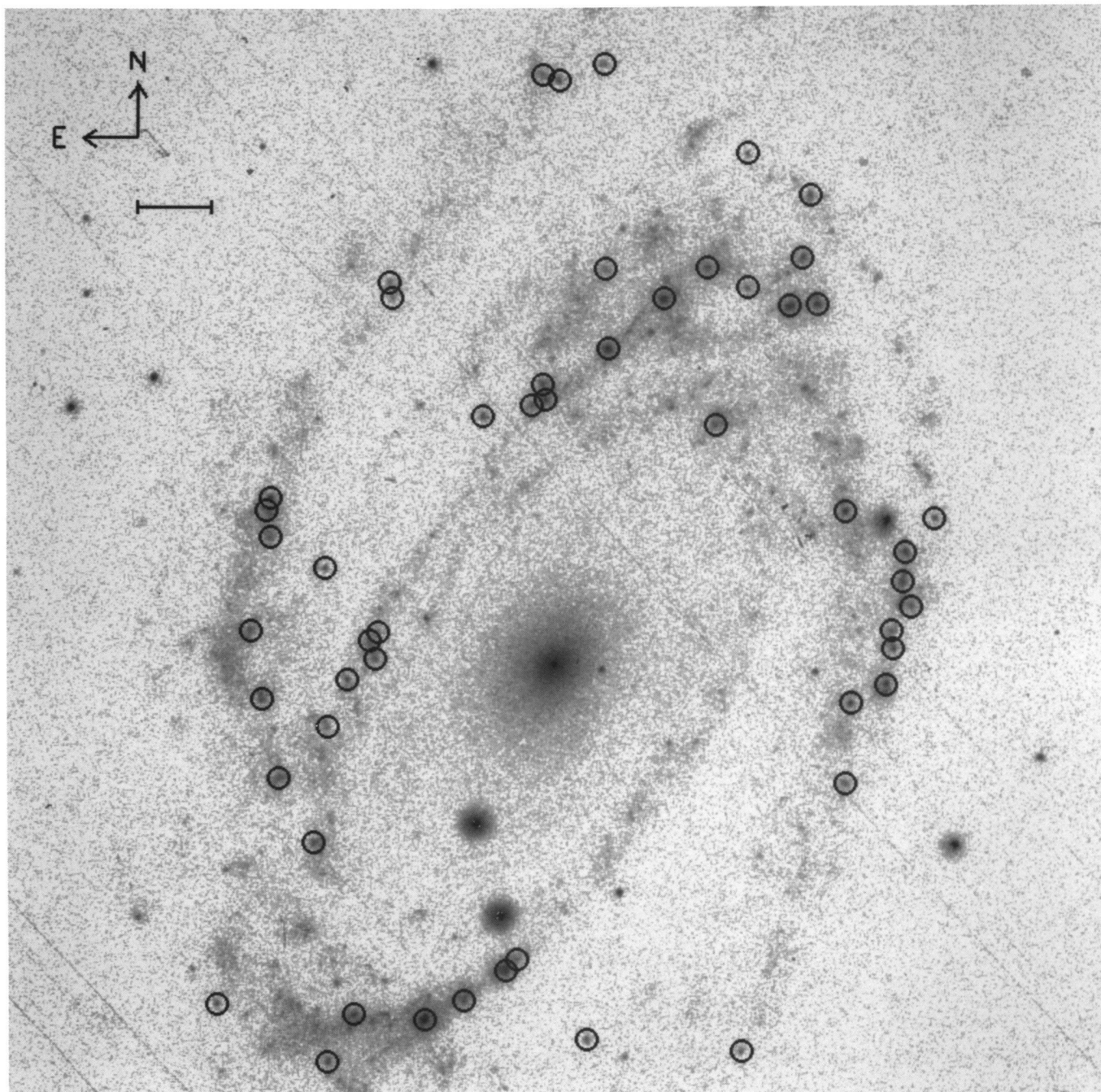
PLATE 9

FIG. 1.—Near-UV UIT A1 band image NUV0442 of M81. North is up, east is to the left. The 52 H II regions discussed are circled
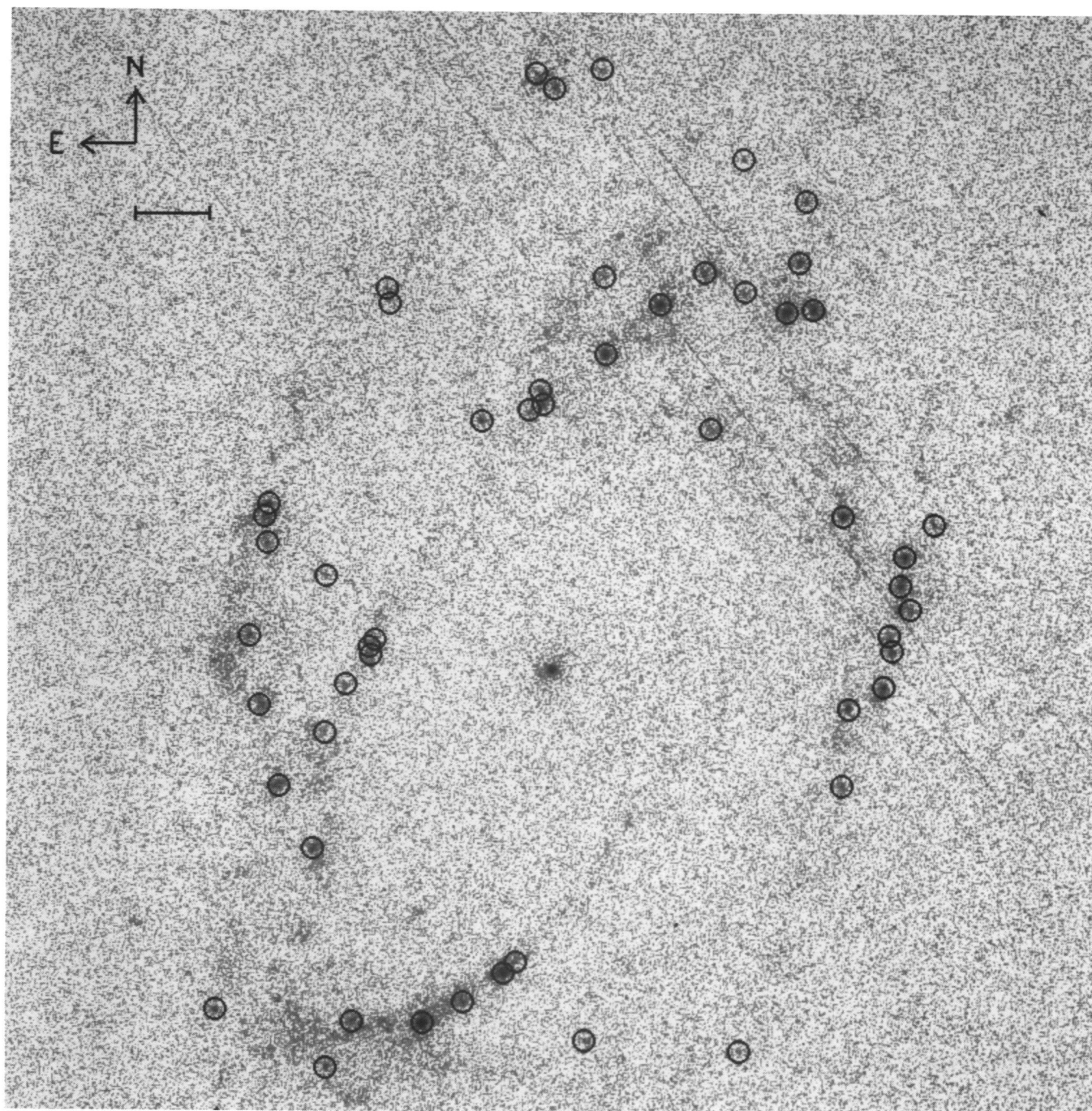
HILL et al. (see 438, 181)

PLATE 10

Fig. 2.—Far-UV UIT B1 band image FUV0556 of M81, registered with F1

Hill et al. (see 438, 181)

TABLE 1

Log of Observatons of M81

Observatory	Telescope	Band	Date	Exposure Time (s)
Astro-1	UIT	B1	1990 Dec 10	639
Astro-1	UIT	A1	1990 Dec 10	640
KPNO	0.9 m	Hα	1991 Mar 13	3 × 600[a]
KPNO	0.9 m	R	1991 Mar 13	3 × 600[a]
Mt. Laguna......	1 m	Hβ	1993 Dec 8	2 × 600[b]
Mt. Laguna......	1 m	4750	1993 Dec 8	3 × 600[a]

[a] Cosmic rays removed by using the median of three images.
[b] Cosmic rays removed by using the minimum of two images.

and outer radii are 11 and 22 arcsec (UV images) or 10 and 20 arcsec (emission line images). When the background on the UV images is less than a critical value, the sky background is taken to be the mean of the pixels in the annulus, rather than the mode, because of the difficulty in linearizing the images near the photographic fog level and the low signal-to-noise there. Aperture photometry is performed using IDL implementations of DAOPHOT algorithms (Stetson 1987).

IUE spectra of isolated stars from several fields observed by UIT determine the UIT calibration, which is accurate to about 10% relative to *IUE*. UIT instrumental fluxes for the calibration are measured through aperture large enough to contain all the stellar flux. UIT magnitudes m are related to fluxes f (in ergs [cm^2 Å s]$^{-1}$) by the relation $m = -2.5 \times \log f - 21.10$. The calibration of the emission line photometry is based on the $\sim 4'' \times 4''$ aperture spectrum scanner measurements of Garnett & Shields (1987). We estimate the uncertainty in the calibration of the emission line fluxes at ~ 10–20%. Our Hα image of M81, with continuum subtracted, is shown in Figure 3 (Plate 11).

The Hα interference filter is of width 61 Å, and includes the [N II] lines. According to Garnett & Shields (1987), the ratio of the [N II] flux to the Hα flux for the seven brightest H II regions is 0.40 ± 0.07. Since the ratio is constant, we calibrate the Hα image directly using the Hα fluxes of Garnett & Shields (1987). The Hα continuum image is in the Kron–Cousins *R*-band, and was scaled to give fluxes equal on average to the instrumental fluxes from the Hα image for the bulge (excluding the nuclear source) and several bright stars before subtracting. The Hβ interference filter is of width 50 Å, as is the corresponding continuum filter, which has central wavelength 4750 Å. The Hβ continuum is scaled and subtracted as in the case of the Hα image.

Continuum magnitudes and emission line fluxes for the H II regions are given in Table 2. For each of the 52 H II regions Table 2 contains the H II region number from PSK (col. [1]), the far-UV magnitude (col. [2]), the estimated error in the far-UV magnitude (col. [3]), the near-UV magnitude (col. [4]), the estimated error in the near-UV magnitude (col. [5]), the Hα flux in 10^{-14} ergs (cm^2 s)$^{-1}$ (col. [6]), the estimated fractional error in the Hα flux (col. [7]), the Hβ flux in 10^{-14} ergs (cm^2 s)$^{-1}$ (col. [8]), and the estimated fractional error in the Hβ flux (col. [9]). For 11 H II regions not measurable in the Hβ line, the Hβ fluxes and the corresponding errors are both set to 0.0. The fractional errors in the line fluxes given in columns (7) and (9) of Table 2 are equal to the estimated flux errors divided by the measured fluxes. The tabulated errors computed by DAOPHOT for the UV magnitudes have been increased by

TABLE 2

M81 H II Region Photometry[a]

PSK	m_{152}	Error	m_{249}	Error	$f_{Hα}$	Error	$f_{Hβ}$	Error
4......	16.14	0.17	17.39	0.12	27	0.05	9.2	0.11
12......	16.32	0.18	17.10	0.12	24	0.05	4.8	0.20
15......	15.70	0.13	16.75	0.11	57	0.05	18	0.05
17......	15.79	0.14	16.63	0.11	44	0.05	8.6	0.10
22......	16.36	0.20	17.58	0.13	8.7	0.06	1.5	0.51
23......	16.12	0.17	17.12	0.12	6.17	0.06	0.0	0.0
22......	15.56	0.12	16.37	0.10	53	0.05	16	0.06
44......	16.04	0.15	17.21	0.12	34	0.05	12	0.09
48......	15.66	0.13	16.58	0.11	39	0.05	14	0.08
52......	16.33	0.18	17.41	0.12	5.0	0.06	0.5	0.90
72......	15.30	0.12	16.33	0.11	27	0.05	5.98	0.19
76......	16.17	0.17	17.38	0.12	4.6	0.09	0.0	0.0
81......	15.78	0.14	16.88	0.11	22	0.05	6.1	0.14
97......	15.06	0.11	16.06	0.10	95	0.05	28	0.04
123......	17.90	0.74	17.92	0.15	4.5	0.07	0.0	0.0
126......	16.75	0.26	18.00	0.15	6.1	0.06	2.7	0.34
134......	16.98	0.30	17.99	0.15	5.3	0.06	3.0	0.30
146......	16.31	0.19	16.91	0.11	8.0	0.06	1.1	0.36
153......	16.03	0.16	17.15	0.11	3.2	0.08	0.0	0.0
178......	15.18	0.12	16.17	0.10	57	0.05	17	0.07
209......	15.21	0.12	16.20	0.10	53	0.05	14	0.07
210......	16.88	0.29	17.71	0.13	8.9	0.19	0.0	0.0
212......	16.56	0.22	17.78	0.13	2.6	0.09	1.5	0.41
221......	16.43	0.19	17.73	0.14	13	0.05	5.7	0.17
228......	16.29	0.20	17.77	0.14	3.4	0.10	0.0	0.0
234......	16.36	0.21	17.71	0.13	2.0	0.62	0.0	0.0
236......	15.78	0.14	16.66	0.11	24	0.05	2.2	0.44
239......	16.21	0.18	16.93	0.11	15	0.05	2.5	0.30
245......	16.67	0.26	17.10	0.12	6.2	0.07	0.7	0.83
261......	15.93	0.15	17.11	0.12	25	0.05	4.1	0.24
266......	14.88	0.11	15.89	0.10	53	0.05	14	0.08
276......	16.16	0.17	17.34	0.12	16	0.05	3.8	0.26
287......	15.87	0.14	16.76	0.11	41	0.05	7.3	0.14
311......	14.42	0.11	15.41	0.11	95	0.05	26	0.05
322......	16.90	0.29	18.01	0.15	27	0.05	9.7	0.11
325......	16.45	0.20	17.77	0.13	7.3	0.06	0.5	0.47
333......	16.19	0.18	17.53	0.13	12	0.05	1.9	0.47
335......	15.68	0.13	17.13	0.12	19	0.05	6.6	0.16
339......	15.66	0.13	16.98	0.11	9.8	0.06	0.0	0.0
362......	16.04	0.15	16.73	0.11	24	0.05	2.1	0.40
366......	16.56	0.21	17.50	0.12	9.2	0.05	0.0	0.0
384......	16.77	0.25	17.79	0.13	8.7	0.05	1.3	0.60
385......	17.18	0.35	18.05	0.15	8.7	0.06	0.0	0.0
388......	16.68	0.22	17.72	0.13	9.3	0.05	0.0	0.0
395......	15.75	0.13	17.15	0.11	16	0.05	6.4	0.17
413......	15.71	0.13	17.01	0.11	1.9	0.12	0.0	0.0
416......	15.92	0.15	16.87	0.11	18	0.05	5.1	0.19
422......	15.83	0.14	16.84	0.11	9.5	0.06	1.9	0.47
424......	16.46	0.21	17.39	0.12	12	0.05	4.5	0.18
438......	15.80	0.14	17.17	0.11	22	0.05	3.9	0.25
442......	16.39	0.19	17.40	0.12	15	0.05	5.5	0.19
472......	16.25	0.17	18.05	0.15	13	0.05	4.6	0.22

[a] Table 2 also appears in the AAS CD-ROM Series, Vol. III.

the addition in quadrature of 0.10 mag for the estimated uncertainty from the characteristic curve and the flat field. For all but the faintest H II regions, the estimated fractional statistical errors in the emission line fluxes are less than the systematic error caused by the uncertainty in the absolute calibration and in the subtraction of the continuum. Table 2 also appears in the AAS CD-ROM Series, Vol. III.

Figure 4 shows the observed UV color-magnitude diagram (CMD) for the M81 H II regions. The error bars are computed from UIT signal-to-noise relation, which is based on the statistics of laboratory flat-field exposures. The brightest six H II regions have measured UV colors with distribution consistent
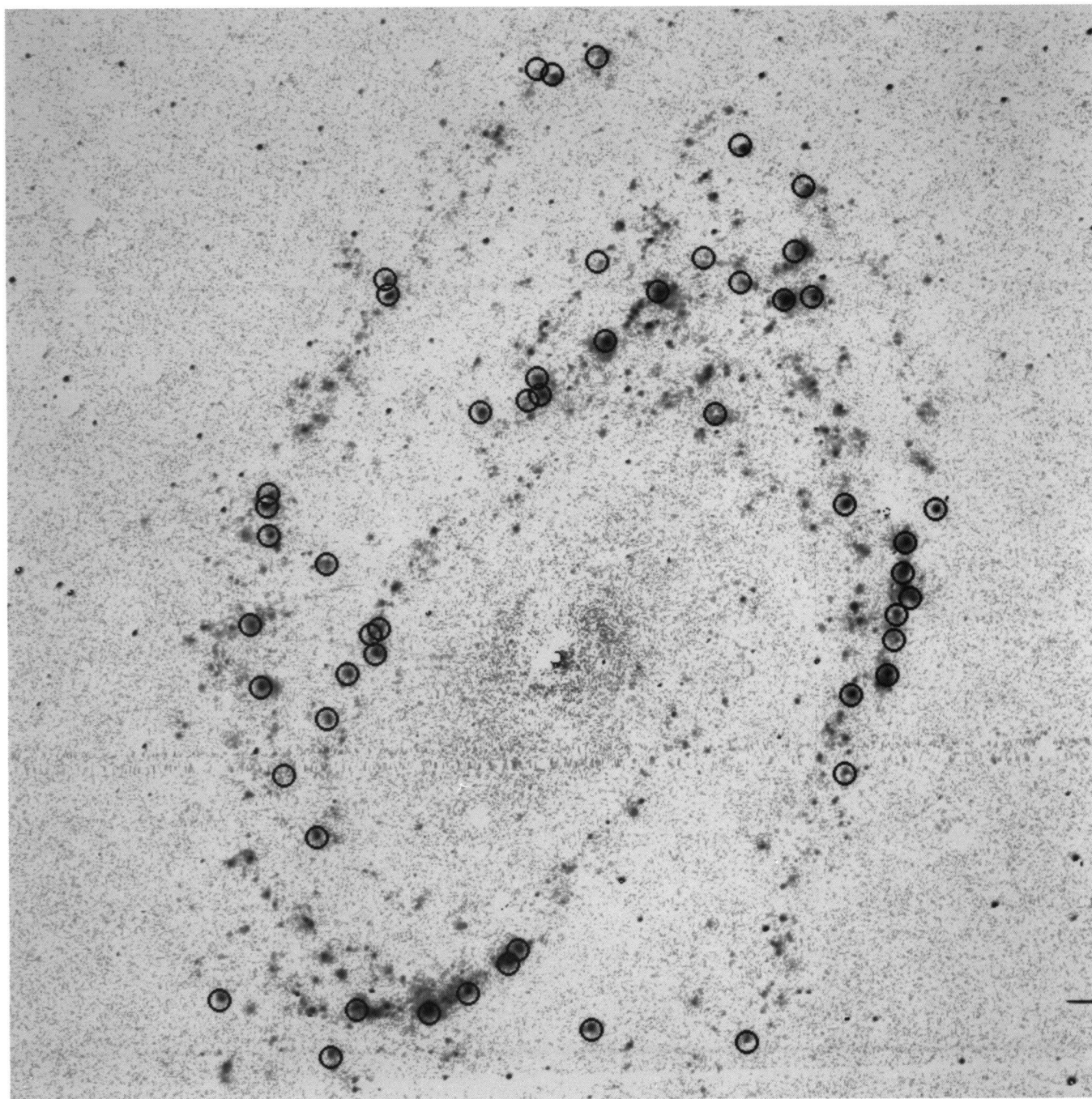
PLATE 11

Fig. 3.—Hα CCD image, registered with Figs. 1–2
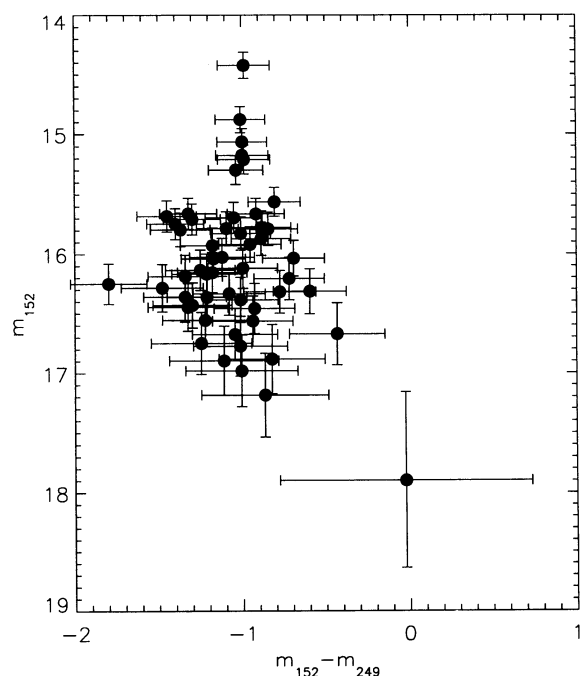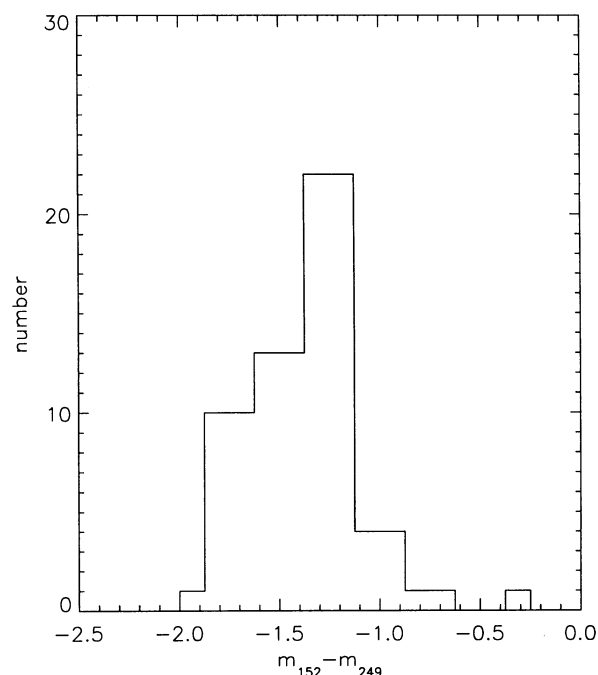
Hill et al. (see 438, 182)

FIG. 4.—UV color-magnitude diagram of the 52 measured H II regions

FIG. 5.—Histogram of observed $m_{152}-m_{249}$ color for the 52 measured H II regions.

with uniform UV color $m_{152}-m_{249} \sim -1.0$. The FWHM of the UV color histogram for all 52 H II regions is ~ 0.3 mag, as shown by the histogram in Figure 5.

A mean Hα extinction of 0.57 mag, with standard deviation 0.17 mag, is computed from the extinctions determined by Kaufman et al. (1987) for the brightest 7 H II regions at Hα using the ratio of the Hα flux to the radio continuum flux at wavelengths 6 cm and 20 cm. Although the spread in Hα extinctions of the seven brightest H II regions is small, some variation in extinction is evident in Figure 6, which plots the Balmer decrement vs. UV color $m_{152}-m_{249}$ for the 22 H II regions with Hβ flux greater than 5.0×10^{-14} ergs (cm² s)$^{-1}$. The observed distribution of Balmer decrement and UV color is probably caused mostly by a spread in extinction affecting both quantities, since the models (described later) predict that the unreddened UV color varies only between -1.46 and -1.20 for ages ranging from zero to 10 Myr, and the Balmer decrement has a weak dependence on the physical conditions (Osterbrock 1989).

The Hα extinction may be determined from the Balmer decrement, if a model for the distribution of the gas and dust is adopted. The most commonly adopted model is the "screen model," in which the dust is located between the source and the observer, and is far enough from the source that scattering back into the beam may be neglected. Use of the screen model to determine extinctions at Hα from the Balmer decrement gives systematically lower Hα extinctions than are obtained by comparing Hα fluxes to radio continuum fluxes (e.g., Caplan & Deharveng 1984).

Instead, we have adopted the models of Witt, Thronson, & Capuano (1992, hereafter WTC), for transfer of radiation in UV, U, B, V, R, and IR bands through a variety of dusty distributions, including absorption and scattering. The "dusty nucleus" models were chosen because the arrangement of radiation sources and dust, namely a dust-free star cluster surrounded by a dust shell, is more similar to the Mathis et al.

(1981) model for the Orion Nebula than any of the other WTC models. The "dusty nucleus" predictions for the relationship between the Hα extinction and the Balmer decrement agree well with the observations of the seven H II regions with the largest observed Hα fluxes (see Fig. 7, *solid line*). The "dusty galaxy" models, for which the stars and dust are co-mixed, also agree well with the observed relation between the Hα extinction and the Balmer decrement. Conversely, the predictions of the foreground screen model (*dashed line*) do not agree with the observations, because the foreground screen model does not include the crucial effects of scattering. The importance of scat-
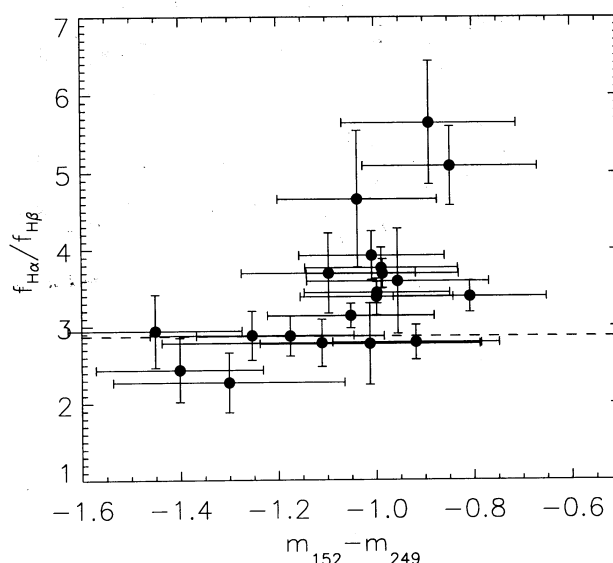
FIG. 6.—UV color $m_{152}-m_{249}$ vs. Balmer decrement. The dashed line shows the assumed unreddened value for the Balmer decrement, 2.87.
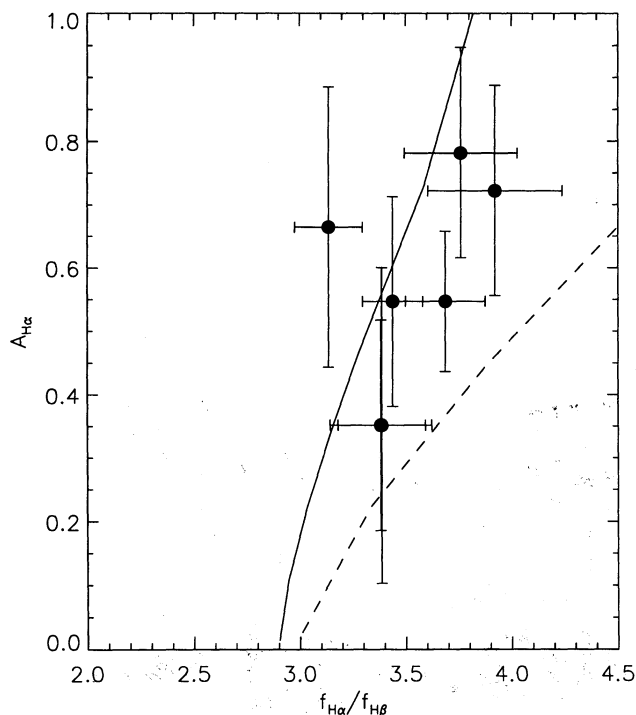
FIG. 7.—Hα extinctions determined by Kaufman et al. (1987) vs. Balmer decrements measured here for seven bright H II regions (*circles*). The solid line is the relationship predicted by the WTC "dusty nucleus" models. The dashed line is the relationship predicted by the foreground screen.

TABLE 3

DERIVED MASSES, AGES, AND EXTINCTIONS FOR M81 H II REGIONS

PSK	Mass $(M_\odot)$	Age (Myr)	$A_{H\alpha}$	A_{152}
4	1900	1.6	0.57	2.38
12	1700	1.5	0.57	2.38
15	4400	1.5	0.66	2.80
17	2900	1.3	0.57	2.38
22	1100	2.6	0.57	2.38
23	2600	3.8	0.57	2.38
29	2800	−1.5	0.32	1.32
44	2300	1.4	0.57	2.38
46	2900	1.7	0.57	2.38
52	2900	4.2	0.57	2.38
72	2900	2.4	0.57	2.38
76	4700	5.0	0.57	2.38
81	2100	2.2	0.57	2.38
97	5300	−1.5	0.37	1.52
123	360	1.8	0.57	2.38
126	750	2.6	0.57	2.38
134	600	2.5	0.57	2.38
146	1200	2.7	0.57	2.38
153	6800	5.6	0.57	2.38
178	2800	−0.4	0.31	1.30
209	5100	2.0	0.63	2.66
210	800	2.1	0.57	2.38
212	3600	5.3	0.57	2.38
221	1200	2.1	0.57	2.38
228	4600	5.2	0.57	2.38
234	5700	5.9	0.57	2.38
236	2200	2.1	0.57	2.38
239	1400	2.2	0.57	2.38
245	820	2.7	0.57	2.38
261	2100	1.9	0.57	2.38
266	8800	2.7	0.77	3.15
276	1500	2.2	0.57	2.38
287	2700	1.3	0.57	2.38
311	8500	2.0	0.57	2.41
322	1700	−0.7	0.57	2.38
325	1000	2.7	0.57	2.38
333	1300	2.4	0.57	2.38
335	2100	2.4	0.57	2.38
339	4700	4.0	0.57	2.38
362	2000	1.8	0.57	2.38
366	950	2.3	0.57	2.38
384	840	2.2	0.57	2.38
385	690	1.8	0.57	2.38
388	910	2.2	0.57	2.38
395	1900	2.6	0.57	2.38
413	14000	6.92	0.57	2.38
416	1800	2.23	0.57	2.38
422	2600	3.36	0.57	2.38
424	1100	2.15	0.57	2.38
438	2100	2.18	0.57	2.38
442	1400	1.98	0.57	2.38
472	1300	2.26	0.57	2.38

tering, as well as the weak dependence of the relation between Balmer decrement and $A_{H\alpha}$ on the details of the source geometry is discussed by Mathis (1983).

We determine the H II extinction from the Balmer decrement for those H II regions with Hβ fluxes greater than 1.0×10^{-13} ergs (cm^2 s)$^{-1}$ and observed Balmer decrements greater than the reddening free value, 2.87 (Osterbrock 1989), using the WTC models. The choice between WTC models "dusty nebula" and "dusty nucleus" is less important for determining the relationship between Hα extinction and the Balmer decrement than for determination of the UV extinction. The "dusty nucleus" model predicts UV extinction 2.38 mag for $A_{H\alpha} = 0.57$ mag, while the "dusty galaxy" model predicts extinction 1.59 mg.

We use the WTC "UVA" band as an analog for the UIT B1 band, because the assumed albedo and phase function asymmetry agree more closely with the findings of Witt et al. (1992) from the UIT observations of NGC 7023 than do the parameters assumed for the WTC "UVB" band. The quotient of the UVA and V extinctions, 2.80, agrees fairly well with that computed for the B1 band from the Galactic extinction curve, 2.69. Derived extinctions for individual regions are given in Table 3.

Correcting UV and Hα fluxes for extinction using the "dusty galaxy" model rather than the "dusty nucleus" model gives dereddened ratios of Lyman continuum flux to far-UV flux larger by about 0.3 in the logarithm. According to the models discussed in § 3, this increase is roughly equivalent to decreasing the age by 2 Myr. Consistent with the geometry of the "dusty nucleus" models, and with observed ratios of Hα flux to far-UV flux, we do not include extinction of the Lyman continuum photon within the H II regions. We conclude that measured Balmer decrements allow the determination of Hα extinctions with little uncertainty from the generally poorly

known geometry. Uncertainties in the geometry affect the UV extinction deduced from the Balmer decrement, leading to uncertainties in the age determined from the ratio of Hα flux to far-UV flux of about 2 Myr. Figure 8 plots the log of the ratio of the Lyman continuum photon flux (computed from the dereddened Hα flux) to the dereddened B1 band flux versus the dereddened B1 band magnitude, where the dereddening is performed using the WTC "dusty nucleus" model.

3. MODEL SEDs

Model spectral energy distributions (SEDs) for young clusters at ultraviolet and visible wavelengths are constructed using the stellar evolutionary models of Schaller et al. (1993)
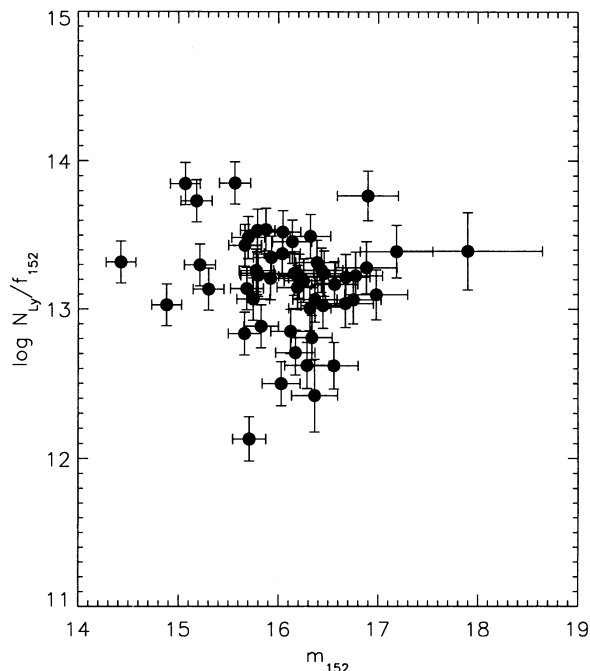
FIG. 8.—Observed log N_{Ly}/f_{152} vs. m_{152} relation for the 52 H II regions.
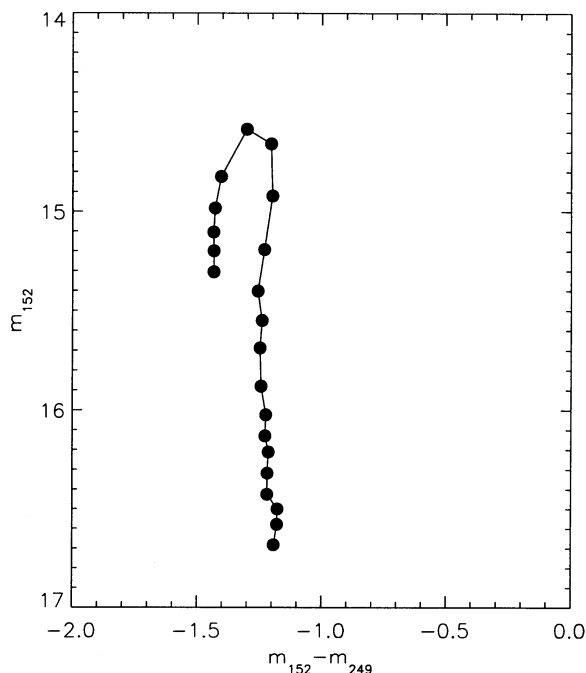

FIG. 9.—Evolutionary track of a young cluster in the UV CMD. The initial point is the blue end, while the age 10 Myr point is at the faint red end. Successive points are separated in time by 0.5 Myr.

together with the model atmospheres of Kurucz (1992), assuming solar abundances. We use the IDL spectral modeling software of Landsman (1992). Spectra were constructed for mass range 5–120 $M_\odot$, IMF slope −1.0 (the Salpeter slope is −1.35), and ages ranging from 0 to 10 Myr, with intervals of 0.5 Myr. The mass range is chosen to include all stars emitting significantly in the Lyman continuum or the far-UV. The adopted IMF slope is near the value −1.08, determined by J. K. Hill et al. (1994) for several OB associations near 30 Dor in the LMC.

Figure 9 shows the evolutionary track of a young cluster in the UV CMD. The cluster initially becomes brighter and sightly redder during the first 3.5 Myr, as the most massive and luminous stars become supergiants. After the maximum luminosity is attained, further evolution is toward fainter magnitudes at approximately constant color. Figure 10 shows the variation of the ratio of the Lyman continuum luminosity (in photon s^{-1}) to the B1 band far-UV luminosity with time. Models with steady state star formation have ratios of Lyman continuum luminosity to far-UV luminosity lower than those of zero age burst models by a factor ∼3.5 (see Fig. 10), because of the contribution of accumulated lower mass and evolved massive stars to the far-UV flux, but not to the Lyman continuum. The value of the ratio of Lyman continuum to far-UV luminosity for an evolving burst becomes equal to the steady state value for age ∼2.5 Myr, and declines for larger ages. The UV colors are similar for the steady state and young burst models, −1.4 for the burst models, and −1.2 for the steady state model, all with IMF slope −1.0.

The degree to which the observed broad-band UV fluxes of galaxies or of small regions within galaxies are dominated by the effects of very recent star formation may be investigated using the ratio of the H II luminosity to the far-UV luminosity. The time since the last significant star formation event may be estimated from this ratio, following the methods of R. S. Hill et al. (1994). We obtain qualitatively similar results from model

SEDs calculated for IMF slopes ranging from −1.0 to −2.0 and upper limit stellar masses ranging from 40 to 85 $M_\odot$. The time dependence of the ratio of the Lyman continuum flux to the far-UV flux is most sensitive to the IMF slope and the upper limit to the stellar mass for ages less than ∼3 Myr, by which time the most massive stars have completed their main
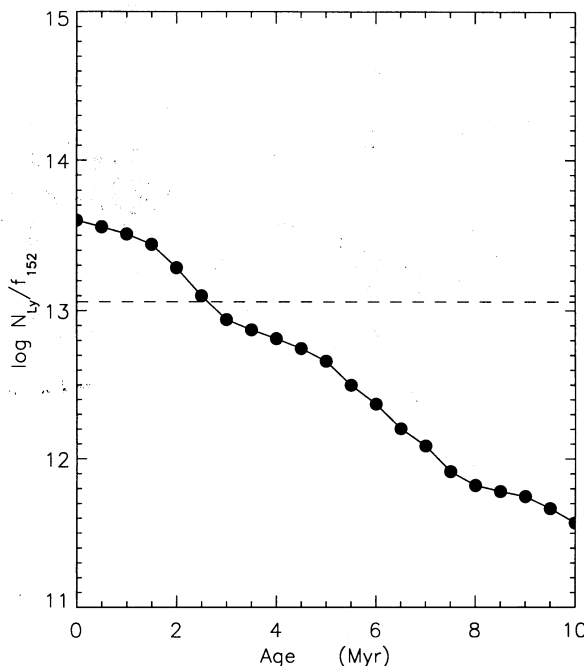

FIG. 10.—Variation of log N_{Ly}/f_{152} with time, for the models. The value of log N_{Ly}/f_{152} for a steady state star-formation model is given by the horizontal dashed line.

sequence lifetimes. The ratios of Lyman continuum flux to far-UV flux agree to within a factor 4 for the different zero-age models, to within a factor 2 for ages larger than 3 Myr.

4. DETERMINATION OF AGES AND MASSES

Ages for the H II regions are estimated from the ratio of the Lyman continuum luminosity to the far-UV luminosity, using the relation plotted in Figure 10, which is smoothed over a time interval 1.5 Myr. We assume that the star formation history of the H II regions is well approximated by the "instantaneous burst" scenario (see R. S. Hill et al. 1994). The computed ages are less than 7.0 Myr, with average value 2.4 Myr. (Small negative ages for 4 H II regions presumably result from observational error in the measurement of the ratio of Hα flux to far-UV flux for very young H II regions.) We estimate the uncertainty in the individual derived ages at ~ 2 Myr. Stellar masses are computed from the relation $M = L_{UV}/\eta$, where M is the total (initial) stellar mass in the range 5–120 $M_\odot$, L_{UV} is the observed B1 band luminosity, corrected for extinction, and η is the far-UV luminosity per $M_\odot$ from the SED models interpolated to the best-fit age. The uncertainty in age of ~ 2 Myr, coupled with an uncertainty of ~ 0.5–1 in the IMF slope leads to an uncertainty in the mass of a factor ~ 5.

Table 3 contains the ages and masses fit from the observed ratios of Hα flux to far-UV flux and from the far-UV flux, as well as the Hα and far-UV extinctions resulting from the analysis above. The masses computed are the total (unevolved) stellar masses, for stars in the range 5–120 $M_\odot$, and range from ~ 380 $M_\odot$ (PSK 123) to $\sim 10^4$ $M_\odot$ (PSK 311, 266, and 413). PSK 413 is noteworthy, because the low ratio of Hα flux to far-UV flux indicates a large age (6.9 Myr), which leads to a large initial far-UV flux and a large mass. PSK 311 is the brightest H II region in the UV and second brightest at Hα. The total of the estimated stellar masses (in the mass range 5–120 $M_\odot$) of all 52 H II regions is 1.4×10^5 $M_\odot$. Figure 11 shows the histogram of estimated H II region masses, which peaks at just over 1200 $M_\odot$. If the same mass function is assumed to apply over the range 0.1–120 $M_\odot$, the estimated masses over the entire range are a factor ~ 2.2 larger than for the smaller range.

Possibly important uncertainties in the models stem from the use of the plane-parallel LTE atmosphres of Kurucz (1992) and the neglect of Lyman continuum extinction within the H II regions. The use of LTE atmospheres does not have a large effect on our models, because for only a small fraction of the lifetime of a massive star is the surface gravity sufficiently low that non-LTE effects are important. Also, the effective temperature is lower for supergiants, which decreases their contribution to the total ionizing flux.

In principle, the neglect of dust absorption in the Lyman continuum is a more serious shortcoming. In effect, we have assumed that any extinction of the Lyman continuum takes place within low solid-angle filaments of high optical depth at both Lyman continuum and far-UV wavelengths, consistent with the optical appearance of, e.g., 30 Dor. The gray extinction of the filaments then has little or no effect on the observed ratio of Hα flux to far-UV flux. Our estimated ages are probably not affected significantly, but our estimated masses are decreased if significant gray extinction by filament exists. If the filaments are of sufficiently low solid angle, this effect is also small. By using the WTC models, we have assumed that the UV extinction follows the Galactic extinction law.

The total of the estimated stellar masses for the 52 observed
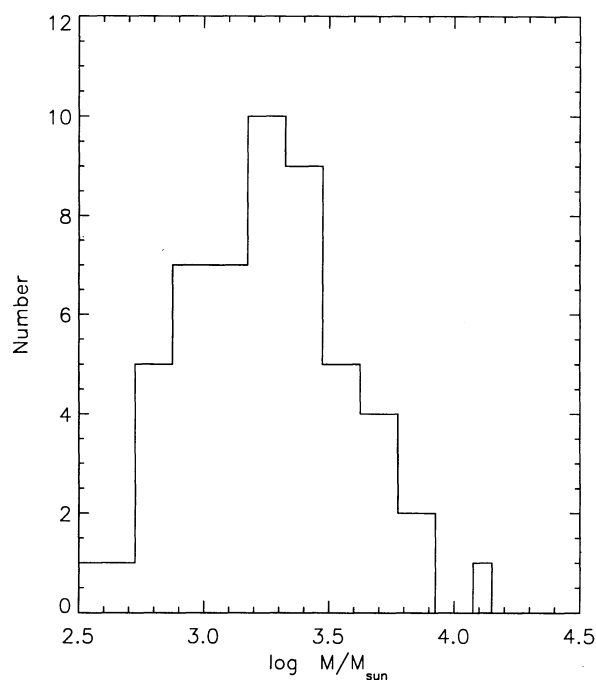

FIG. 11.—Histogram of the estimated masses for the 52 H II regions in bins of width 0.15 in the log of the estimated mass. The masses are the total initial stellar masses in the range 5–120 $M_\odot$.

H II regions is 3×10^5 $M_\odot$, including the low-mass stars. This mass may be used together with the average estimated age of 2.4 Myr to compute a lower limit to the total star-formation rate in M81 of 0.13 $M_\odot$ yr^{-1}. The actual total star formation rate in M81 is unlikely to be greater than this limit by more than a factor 5, since this is the range spanned by models employing IMF slopes varying from -1.0 to -2.0. The factor by which the total of Hα fluxes for the 492 H II regions measured by PSK is greater than the total for the 52 H II regions measured here is only ~ 1.2. The inferred low total star-formation rate 0.13 $M_\odot$ yr^{-1} for M81 is typical for early-type spiral galaxies, according to Kennicutt (1983) and Caldwell et al. (1991).

5. SUMMARY

Extinction-corrected Hα and far-UV fluxes of individual H II regions within spiral or irregular galaxies may be used to estimate the age and total mass of the associated stars. Hα extinctions may be determined from observed Balmer decrements using the radiative transfer models of WTC. UV extinctions may be estimated from the same models, if the geometry of the local dust distribution is known or assumed. The star formation rate of the early-type Sab spiral galaxy M81 observed in the UV during the Astro-1 Spacelab mission by the Ultraviolet Imaging Telescope is ~ 0.1–0.2 $M_\odot$ yr^{-1}.

REFERENCES

Bohlin, R. C., Cornett, R. H., Hill, J. K., O'Connell, R. W., & Stecher, T. P. 1990a, ApJ, 352, 55
Bohlin, R. C., Cornett, R. H., Hill, J. K., & Stecher, T. P. 1990b, 363, 154
Caldwell, N., Kennicutt, R., Phillips, A. C., & Schommer, R. A. 1991, ApJ, 370, 526
Caplan, J., & Deharveng, L. 1986, A&A, 155, 297
Garnett, D. R., & Shields, G. A. 1987, ApJ, 317, 82
Hill, J. K., et al. 1992, ApJ, 395, L37
Hill, J. K., Bohlin, R. C., & Stecher, T. P. 1984, ApJ, 277, 542
Hill, J. K., Isensee, J. E., Cornett, R. H., Bohlin, R. C., O'Connell, R. W., Roberts, M. S., Smith, A. M., & Stecher, T. P. 1994, ApJ, 425, 122
Hill, R. S., Home, A. T., Smith, A. S., Bruhweiler, F. C., Cheng, K.-P., Hintzen, P. M. N., & Oliversen, R. J. 1994, ApJ, 430, 568
Hodge, P. W., & Kennicutt, R. C. 1983, AJ, 88, 296
Kaufman, M., Bash, F. N., Kennicutt, R. C., & Hodge, P. W. 1987, ApJ, 319, 61
Kennicutt, R. C. 1983, ApJ, 272, 54

Kurucz, R. L. 1992, in The Stellar Populations of Galaxies, ed. B. Barbuy & A. Renzini (Dordrecht: Kluwer), 225
Landsman, W. B. 1992, private communication
Mathis, J. S. 1983, ApJ, 267, 119
Mathis, J. S., Perinotto, M., Patriarchi, P., & Schiffer, F. H. 1981, ApJ, 249, 99
O'Connell, R. S., et al. 1992, ApJ, 395, L45
Osterbrock, D. E. 1989, Astrophysics of Gaseous Nebulae and Active Galactic Nuclei (Mill Valley, CA: University Science Books)
Petit, H., Sivan, J. P., & Karachentsev, I. D. 1988, A&AS, 74, 475 (PSK)
Sandage, A. 1984, AJ, 89, 621
Schaller, G., Shaerer, D., Maynet, G., & Maeder, A. 1992, A&AS, 96, 269
Stauffer, J. R., & Bothun, G. 1984, AJ, 89, 1702
Stecher, T. P., et al. 1992, ApJ, 395, L1
Stetson, P. B. 1987, PASP, 99, 101
Witt, A. N., Thronson, H. A., & Capuano, J. M. 1992, ApJ, 393, 611 (WTC)